A single *Leishmania* adenylate forming enzyme of the ANL superfamily generates both acetyl- and acetoacetyl-CoA

Andrew J. Jezewski[1], Taiwo E. Esan[2], Jonah Propp[1], Andrew J. Fuller[1], Drashti G. Daraji[2], Charles Lail III[2], Bart L. Staker[3,4], Elijah L. Woodward[5,4], Linjun Liu[5,4], Kevin P. Battaile[6], Scott Lovell[5,4], Timothy J. Hagen[2], and Damian J. Krysan*[1,7]

[1]Department of Pediatrics Carver College of Medicine, University of Iowa, Iowa City, IA 52242

[2]Department of Chemistry and Biochemistry, Northern Illinois University, DeKalb, Illinois, 60115

[3]Center for Global Infectious Disease Research Seattle Children's Research Institute, Seattle, WA 98109

[4]Seattle Structural Genomics Center for Infectious Disease (SSGCID), Seattle, Washington, 98109, USA

[5]Del Shankel Structural Biology Center University of Kansas, Lawrence, KS 66047

[6]NYX, New York Structural Biology Center, Upton, NY 11973

[7]Microbiology/Immunology, Carver College of Medicine, University of Iowa, Iowa City, IA 52242

Running title: Leishmania encodes dual function ACS/KBC enzyme.

Keywords: acetyl-CoA synthetase, acetoacetate, Leishmania, metabolism, substrate specificity

Corresponding Author:

Damian J. Krysan

2040 Med Labs 25 S. Grand Avenue, Department of Pediatrics and Microbiology/Immunology, Carver College of Medicine, University of Iowa, Iowa City Iowa 52242, Phone: 319-335-3066, damian-krysan@uiowa.edu

Abstract (250 words)

Leishmania, a protozoan parasite, is responsible for significant morbidity and mortality worldwide, manifesting as cutaneous, mucocutaneous, and visceral leishmaniasis. These diseases pose a substantial burden, especially in impoverished regions with limited access to effective medical treatments. Current therapies are toxic, have low efficacy, and face growing resistance. Understanding the metabolic pathways of *Leishmania*, particularly those differing from its host, can unveil potential therapeutic targets. In this study, we investigated the acetyl-CoA synthetase (ACS) enzyme from *Leishmania infantum* (*Li*Acs1), which, unlike many organisms, also exhibits acetoacetyl-CoA synthetase (KBC) activity. This dual functionality is unique among ANL superfamily enzymes and crucial for the parasite's reliance on leucine catabolism, energy production and sterol biosynthesis. Our biochemical characterization of *Li*Acs1 revealed its ability to utilize both acetate and acetoacetate substrates. Additionally, *Li*Acs1 displayed a distinct CoA substrate inhibition pattern, partially alleviated by acetoacetate. Structural analysis provided insights into the substrate binding flexibility of *Li*Acs1, highlighting a more promiscuous substrate pocket compared to other ACS or KBC-specific enzymes. Substrate mimetics elucidated its ability to accommodate both small and large AMP-ester derivatives, contributing to its dual ACS/KBC functionality. These findings not only advance our understanding of Leishmania metabolism but also present *Li*Acs1 as a promising drug target. The dual functionality of *Li*Acs1 underscores the potential for developing selective inhibitors that could disrupt critical metabolic pathways across *Leishmania* spp. as it appears this enzyme is highly conserved across this genus. This paves the way for developing novel effective treatments against this devastating disease.

Introduction

Leishmania is a protozoan parasite responsible for causing disease that manifests as skin ulcers called cutaneous leishmaniasis (CL), ulcers of the nose, mouth, and throat called mucocutaneous leishmaniasis (MCL), or the more severe organ damage associated visceral leishmaniasis (VL). World-wide, up to 400 thousand cases of CL and 1.2 million cases of VL contribute to nearly 40 thousand deaths annually (1). Together, *Leishmania* spp. are the biggest parasitic killers after the malaria causing parasites. Perhaps as alarming as Leishmaniasis mortality is its morbidity. Survivors of CL frequently face life-long disfigurement, and, in many cultures, this disability serves as a pre-text for exclusion from society (2). The global distribution of *Leishmania* puts 350 million at risk for this devastating disease in primarily impoverished regions with lack of access to medical care (3). As a eukaryotic pathogen and parasite, *Leishmania* presents unique challenges for treatment. Current therapies include highly toxic and low efficacy options such as pentavalent antimonials, miltefosine, amphotericin B (AmB), and paromomycin. Additionally, each of these therapies are difficult to access and are vulnerable to a growing threat of drug resistance and treatment failure (4). The limited range of treatments, coupled with their significant adverse effects, underscores the urgent need for new therapeutic strategies.

Leishmania is transmitted to humans through the bite of an infected female phlebotomine sandfly. These sandflies are tiny and therefore difficult to see. They are also most active during sleeping hours and particularly resistant to vector control measures; including broad application of insecticides and insecticide treated nets (5). Upon infection, this parasite undergoes a morphological change from the flagellated promastigote found in the sandfly to the non-flagellated amastigote in mainly macrophages but also other mononuclear phagocytic cells. The lifecycle completes upon uptake from a sandfly taking a subsequent blood meal and morphogenesis back to the promastigote form (6). *Leishmania* has evolved distinct metabolic adaptations given the unique life cycle and transitioning between sandfly and mammalian hosts. Strategies for nutrient acquisition, availability of carbon and nitrogen sources, and the biosynthetic needs for proliferation and morphogenesis each require unique metabolic demands (7–10). Understanding the metabolic pathways, especially those that differ from its host, can provide insights into potential therapeutic strategies that target processes crucial for the parasite's survival and pathogenicity.

In general, the trypanosomatids which include *Leishmania* spp., exhibit an elevated reliance on leucine catabolism for energy production and sterol biosynthesis compared to their mammalian hosts (11). Sterols present a unique metabolic target in the trypanosomatids as this is the metabolic target of one of the few anti-trypanosomal therapies, AmB. Like fungi, trypanosomes require ergosterol, the target of AmB, while mammals require cholesterol to maintain proper membrane function (12). Across mammals, fungi, and trypanosomes, the parent sterol generating mevalonate (MVA) metabolic pathway is conserved; however, like the differences in sterol products, the metabolic flux into sterol biosynthesis is distinct. In mammals, the MVA pathway is predominantly supplied carbon equivalents via ATP-citrate lyase (ACL) generated acetyl-CoA (13). Similar to many parasitic protozoa, *Leishmania* require acetyl-CoA synthetase (ACS) function for acetyl-CoA production. The lack of alternative viable acetyl-CoA producing pathways in the cytosol underlie the essentiality of ACS in *Leishmania* (14).

Leucine catabolism generates two carbon molecules that contribute to sterol biosynthesis: 1] acetyl-CoA and 2] acetoacetate. Acetyl-CoA can directly feed into the MVA pathway. Specifically, the first step of the MVA pathway involves acetoacetyl-CoA production via condensation of two acetyl-CoA molecules to form acetoacetyl-CoA. In addition, some organisms encode a second ACS like enzyme called acetoacetyl-CoA synthetase or 3-keto-butanoyl-CoA synthetase (KBC) after the systematic IUPAC name of acetoacetate (15–19). These enzymes allow direct synthesis of acetoacetyl-CoA from acetoacetate and CoA. Curiously, *Leishmania* spp. lack a separately encoded bona fide KBC despite a high reliance on leucine catabolism and therefore elevated production of acetoacetate (Figure 1A). We report that the ACS encoded by *Leishmania infantum* is a novel dual substrate enzyme and serves both ACS and KBC functionality. ACS homologs are highly conserved across *Leishmania* spp., suggesting that this dual function may also be conserved.

Uncovering a dual function ACS provides new insight into the structural and biochemical features of **A**cyl-CoA/**N**RPS/**L**uciferase (ANL) family enzymes that will aid the pursuit of ACS as a drug target beyond the fight against Leishmaniasis. Parasites, fungi, and bacteria exhibit similar metabolic vulnerabilities and have been shown to require ACS functionality during infection (17). Additionally, many cancers in humans show a dependence on ACS, making it a focal point in developing anti-cancer therapies. Expanding our insight into the substrate binding selectivity of ACS could guide the design of disease specific inhibitors while reducing side effects that may result from off-targeting other ANL family enzymes.

Results

Leishmania spp. lack expression of a KBC via sequence homology detection.

A homology detection strategy was implemented using a standard BLAST search of short acyl-CoA forming enzymes, specifically ACS or KBC like enzymes encoded by *Leishmania* spp. We used previously characterized ACSs and KBCs as reference enzymes (name:uniprot IDs) from humans (*Hs*Acss2: Q9NR19, *Hs*Aacs: Q86V21), *Streptomyces* (*Sl*Acs1: A0A7U9HBW6, *Sl*Aacs: A0A7U9DRD6), *Cryptococcus* (*Cn*Acs1: J9VFT1, *Cn*Kbc1: J9VT24), and the model yeast *Saccharomyces* (*Sc*Acs1: Q01574, *Sc*Acs2: P52910) (15, 17, 18, 20–23). We identified two copies of short length acyl-CoA forming enzymes for *L*. *infantum* (*Li*Acs1: A4I093, *Li*Acs2: A4I0C2), *L*. *donovani* (*Ld*Acs1: E9BG78, *Ld*Acs2: A0A3S7WXN0), *L*. *braziliensis* (*Lb*Acs1: A4HCR9, *Lb*Acs2: A4HCU1), and only a single copy in *L. amazonensis* (*La*Acs1: LAMA_000440100.1) as identified by its EuPathDB ID. Close inspection of the *La*Acs1 annotated reading frame showed an error such that only residues 282-615 are currently annotated for a 705 amino acid reading frame. The full-length protein was considered in these studies. We compared sequences using the multiple sequence protein alignment algorithm ClustalOmega along with the previously mentioned reference enzymes (24–27). The percent identity matrix and sequence clustering indicate that all *Leishmania* spp. enzymes group with previously characterized ACS enzymes and are more distantly related to KBC functioning enzymes (Figure 1B). Among the encoded *Leishmania* ACS candidates, the sequence homology exceeds 83% identity within species and 78% across species, indicating a higher conservation of function than is seen in yeast, where *Sc*Acs1 and *Sc*Acs2 only share 54% identity despite shared substrate preference. Conversely, these *Leishmania* ACS candidates exhibit less than 25% identity compared to other KBC functioning enzymes, whereas mammals, yeast, and prokaryotes exhibit >37% identity across their encoded KBCs.

*Li*Acs1 exhibits dual ACS and KBC functionality.

To characterize the biochemical and enzymatic properties of *Li*ACS we expressed an N-terminal His8-tagged fusion protein in *E. coli* and purified by immobilized metal affinity chromatography (IMAC) and size exclusion chromatography (SEC) (Figure 2A). X-ray crystal structures of ACSs from other species adopt a trimeric form; however, these studies have not assessed oligomer formation using solution based analyses (22). To assess the oligomeric state and particle size of *Li*ACS as well as previously studied *Cn*Acs1 and *Cn*Kbc1, we performed dynamic light scattering and single molecule analysis using mass photometry (17, 22). In agreement with previous crystallography, *Cn*Acs1 forms a particle size consistent with trimer formation at 1mg/mL (Table 1) and this trimer is stable at low particle density (227 ± 7.8 kDa at 10nM, Figure 2B). Similarly, *Cn*Kbc1, which has not been structurally characterized, exhibits a particle size consistent with trimer formation at 1mg/mL (Table 1) that is also stable at low particle density (226 ± 7.4 kDa at 10nM, Figure 2C). This is in contrast to *Li*Acs1 which shows no detectable trimer formation under either high concentrations 1mg/mL (Table 1) or during single molecule analysis at low concentrations (74 ± 7.8 kDa at 10nM, Figure 2A).

To biochemically characterize *Li*Acs1, we employed a coupled continuous assay based on pyrophosphate-release as previously reported for detecting various acid substrate utilization in the production of their respective acyl-CoA products (17). The specific activity for acetate utilization was 960 nmol/min/mg, which is far higher than our previously reported ACS enzymes ranging from 12-836 nmol/min/mg corresponding to a catalytic efficiency of $K_{cat}^{app}/K_{m}^{app}$ = 20 $mM^{-1}s^{-1}$ (Figure 3A) (22). Loss of activity was observed below pH 6.0 as has been previously described for ACS enzymes (Figure 3B). To characterize (or determine) the substrate selectivity of *Li*Acs1, we compared the activity of six carboxylic acid substrates: acetate, propionate, butyrate, acetoacetate, 3-hydroxybutyrate, and valerate (smallest to largest). Unlike previously characterized ACSs, *Li*Acs1 exhibits both acetate and acetoacetate substrate utilization with minimal 3-hydroxybutyrate activity (15 % of V_{max}) and no appreciable activity for the remaining acid substrates (Figure 3C). While the pyrophosphate dependent enzyme activity detection assay only measures the first half of the reaction, intermediate product formation is not released in the absence of CoA and the reaction only progresses when CoA is present (28). To be sure that acyl-CoA products form successfully in the presence of either acetate or acetoacetate we also performed a hydroxamate detection assay where hydroxylamine reacts with acyl-CoA in the presence of iron to form a hydroxamate product that absorbs at 560nm (29, 30). We confirm acetyl-CoA and acetoacetyl-CoA formation using this well-established assay (Supplemental Figure 1). To be sure that hydroxamate formation was not occurring with the acyl-AMP intermediate we performed the reaction without CoA to assure hydroxylamine itself was not serving as an electron acceptor and that acyl-AMP release was not occurring in its presence. Together, these data indicate that *Li*Acs1 is an acyl-CoA synthetase that utilizes both acetate and acetoacetate substrates.

_Li_Acs1 exhibits strong CoA substrate inhibition that is partially relieved by acetoacetate.

ACSs function with an ordered bi-uni-uni-bi ping pong reaction mechanism where ATP binds first and is followed by acetate (31). These substrates are then catalyzed to form the acetyl-AMP reaction intermediate in the adenylate forming conformation (AD-conf) while inorganic pyrophosphate is released (22, 32). The enzyme then undergoes a conformational shift to allow CoA binding in the thioester forming conformation (TE-conf), where the acetyl group from acetyl-AMP is transferred to CoA to form acetyl-CoA (22, 32). Finally, the acetyl-CoA and AMP are released. We were curious if the dual acid substrate utilization of *Li*Acs1 would result in altered substrate binding affinity compared to other ACS or KBC functioning enzymes; however, both ATP (K_m^{app} = 230 μM, CI (95%) = (190, 270)) and acetate (K_m^{app} = 61 μM, CI (95%) = (45, 83)) exhibited similar kinetics with K_m^{app}'s comparable to previously characterized ACSs (Figure 4A-B) (20, 22, 23). Likewise, acetoacetate exhibited a K_m^{app} (88 μM, CI (95%) = (71, 110)) comparable to the K_m for previously reported KBCs (Figure 4C) (17). Enzyme kinetics did uncover a mild ATP substrate inhibition yielding higher theoretical V_{max} = 1.8 μmol/min/mg, CI (95%) = (1.6, 2.0) not discernible from the acyl or CoA substrate enzyme activity curves. The substrate inhibition for ATP corresponded to a K_i^{app} = 2.2 µM, CI (95%) = (1.7, 2.7).

Despite exhibiting dual substrate specificity of *Li*Acs1, we did not observe an appreciable decrease in its affinity for either acetate or acetoacetate compared to other ACS and KBC enzymes, respectively. Interestingly, *Li*Acs1 displays stark CoA substrate inhibition that is uncharacteristic of previously described ACS enzymes and more pronounced than previously reported KBCs (Figure 4D) (17). We fit a nonlinear regression model for substrate inhibition using GraphPad Prism, which indicates a K_i^{app} = 262 µM, CI (95%) = (110, 460) close to the K_m^{app} = 265 µM, CI (95%) = (150, 620) for CoA with a V_{max} = 2.4 µmol/min/mg, CI (95%) = (1.7, 4.9) (Figure 4D). The level of CoA substrate inhibition is far more pronounced than was previously described for *Cn*Kbc1 based on the observation that $K_i^{app} \approx K_m^{app}$. Surprisingly, we observed a dramatic reduction in CoA inhibition when the substrate is acetoacetate rather than acetate (K_i^{app} = 891 µM, CI (95%) = (600, 1275); K_m^{app} = 171 µM, CI (95%) = (120, 250); V_{max} = 2.5 µmol/min/mg, CI (95%) = (2.1, 3.1) where $K_i^{app} > K_m^{app}$. This relationship between K_i^{app} and K_m^{app} in the presence of acetoacetate is similar to the CoA substrate inhibition measured for *Cn*Kbc1 (17). The differences This suggests that small acid substrate binding to *Li*Acs1 in the first half of the ACS reaction influences CoA binding characteristics in the second half of the reaction.

_Li_Acs1 substrate pocket accommodates both large and small AMP-ester bi-substrate inhibitors.

Acetyl-CoA synthetases are differentiated from KBCs, medium-chain, and long-chain acyl-CoA synthetases by the presence of a stable Tryptophan wall, which prevents larger acyl substrates from entering the pocket. Given that *Li*Acs1 contains this ACS-like tryptophan residue (W466) we were surprised to observe acetoacetate utilization. The utilization of both acetate and acetoacetate suggests that *Li*Acs1 contains a more promiscuous substrate binding pocket compared to ACS and KBC specific enzymes. We and others have used AMP-ester based, bi-substrate inhibitors of ACS, KBC and ANL-family enzymes to characterize the alkyl group sizes accommodated by the different enzymes (17, 22, 33–35). We generated a series of AMP-esters with different alkyl chain lengths, alkyl branching, and degrees of unsaturation. The inhibitors mimic the acyl-AMP intermediate following the first half of the reaction. These bi-substrate mimetics allow us to probe the small acid substrate pocket by assessing their ability to bind and inhibit the reaction from progressing.

The profile of inhibition across these various sized and shaped AMP-esters can help us assess the flexibility of the small acid substrate binding pocket for *Li*Acs1 compared to the acetate specific *Cn*Acs1 vs acetoacetate specific *Cn*Kbc1 enzymes. By organizing the AMP-esters according to their Van der Waals volume from smallest to largest (from left to right) we can directly compare size vs ability to inhibit enzyme activity plotted as the -log10 IC_{50} (μM) such that a higher value corresponds to an increase in inhibitor potency (Figure 5, Table 2). While IC_{50} is substrate concentration dependent, it can be used to as a proxy to compare relative Ki's for inhibitors to a given enzyme when assay conditions hold substrate concentrations constant (36). The inhibition profile of the acetate specific *Cn*Acs1 shows a peak in inhibition for the ethyl- and cyclopropyl-AMP derivatives with a ~3-fold drop in inhibition for the propyl- and isopropyl-AMP derivatives and another ~2-fold drop in inhibition for the allyl- and propargyl-AMP derivatives (Figure 5, Table 2). This steady decrease in inhibition as AMP-ester derivatives increase in size indicates *Cn*Acs1 contains a substrate binding pocket that selects for relatively smaller alkyl substituted carboxylic acid substrates. Conversely, the acetoacetate specific *Cn*Kbc1 exhibits a more restrictive substrate binding pocket such that only the larger sized butyl-AMP ester exhibits any inhibition (Figure 5, Table 2).

Consistent with its "hybrid" substrate specificity, the AMP-ester inhibition profile for *Li*Acs1 is a composite of the *Cn*Acs1 and *Cn*Kbc1 profiles such that the peak inhibition occurs with ethyl- and cyclopropyl-AMP derivatives with a ~3 to 6-fold drop in inhibition for the propyl- and isopropyl-

AMP derivatives that does not drop again for the larger allyl- and propargyl-AMP derivatives (Figure 5, Table 2). While *Li*Acs1 can accommodate the larger allyl- and propargyl-AMP derivatives much better than *Cn*Acs1 it does not extend to butyl-AMP as occurs for *Cn*Kbc1. Together, the AMP-ester inhibition profile for *Li*Acs1 does confirm a more flexible substrate binding pocket that, in turn, likely allows for both acetate and acetoacetate utilization and therefore dual ACS/KBC functionality.

_Li_Acs1 structure is highly homologous to previous ACS structures.

To understand the structural basis for substrate specificity, we performed x-ray crystallography and successfully obtained several structures of *Li*Acs1. We were able to generate structures in complex with combinations of CoA, AMP, acetate, and/or ethyl-AMP. The AMP-acetate/CoA structure is similar overall to *Cn*Acs1 (PDB: 7L4G) with an RMSD deviation of 1.26 Å between Ca atoms (511 residues). Previously, our group reported the crystal structures for *Cn*Acs1 across each step of the enzyme reaction (22). Consistent with previous structural and biochemical analyses of adenylating enzymes, the structures highlighted a massive conformational shift that occurs in the C-terminal domain (CTD) domain between the first half of the reaction in the adenylate (AD-conf) forming step to the thioester (TE-conf) forming second half of the reaction. We captured *Li*Acs1 in the TE-conf in the presence of CoA, AMP, and acetate (Figure 6A). The CoA molecule in *Li*Acs1 is located at an interface between the N- and C-terminal domains and interacts with the side chains of K240, R237 and R636 and is engaged with the substrate pocket consistent with previous CoA bound ACS structures (Figure 6B). However, the pantetheine tail of the CoA molecule was disordered and could not be modeled. We were also able to capture a unique state of the adenylate forming pocket with the AMP molecule present with an acetate in the active site. AMP forms hydrogen bond interactions with D463, T464, Q467, T468, D552, R567 and R578 while the acetate molecule appears to remain in contact the phosphate group of AMP. This is a very unusual finding because the presumed mechanism for generation of the acetyl-

AMP intermediate of the first reaction is through nucleophilic attack of the acetate on the phosphate of ATP to displace pyrophosphate. ATP and acetate have been shown to bind in an ordered fashion such that the ATP binding event allows for acetate binding. Our structure suggests that the acetate binding pocket is not solely dependent on ATP but rather AMP is sufficient to allow acetate binding, although our crystallization conditions include 200 mM acetate which could preclude any mechanistic explanation for this binding. No previous ACS structure has shown the acid substrate bound alone and the current structures support an ordered binding event. Hydrogen bond interactions and electron density maps for the ligands are shown in Figure 6 B-D.

The structure without acetate bound displays a high degree of similarity compared to the ATP-acetate/CoA bound structure with an RMSD deviation of 0.27 Å between Ca atoms (661 residues). Despite the absence of the acetate molecule AMP adopts a nearly identical binding mode with only a small shift in the phosphate group as shown in Supplemental Figure 2A. We also generated crystals without acetate but in the presence potassium bromide or potassium thiocyanate. These yielded a structure with a potassium ion bound near the AMP molecule and generated very similar structures to the acetate bound and unbound crystals with an RMSD deviation of 0.39 Å between Ca atoms (660 residues). The main difference found in the potassium bound structure occurs in the loop containing residues G576 and N573 which is moved away slightly from the AMP molecule. This results in a new contact between AMP and N573 which also coordinates the potassium ion (Supplemental Figure 2B).

***Li*Acs1 acid substrate pocket is wider than the acetate restricted *Ca*Acs2.**

To better understand any differences that might exist for substrate binding between the dual substrate binding acetate/acetoacetate utilizing *Li*Acs1 and an acetate restricted *Candida albicans* Acs2 (*Ca*Acs2) (PDB: 8V4R) we also crystallized *Ca*Acs2 in the presence of AMP, acetate, and CoA (22). It is clear that the *Li*Acs1 exhibits an alternative binding orientation for acetate (Supplemental Figure 4A) compared to *Ca*Acs2 (Supplemental Figure 4B). At first look, the AMP, acetate containing substrate pockets are not large enough to accommodate acetoacetate. However, the binding pose of AMP relative to the pocket shows a 1.5 Å greater distance between the proximal oriented phosphate of AMP and the classic substrate size restricting tryptophan wall (W466) (Figure 7A-B). About half of this distance can be attributed to orientation of the phosphate oxygens as the distance from phosphorous atom to the tryptophan wall is 8.7 Å for *Li*Acs1 versus 8.1 Å for *Ca*Acs2. Further pocket widening may occur with substrate accommodation as our previously reported *Cn*Acs1 crystal structures highlighted a slight pocket widening that occurs for AMP-ester bi-substrate mimetics. Our and others' previous studies have illustrated substrate restriction occurs through the presence of a stable Tryptophan wall that prevents larger substrates from being accommodated (22, 37). Pocket widening does occur opposite to this tryptophan wall and appears to be determined largely by the overall flexibility of the CTD. This pocket widening can be seen in the previously reported *Cn*Acs1 in complex with ethyl-AMP (Supplemental Figure 4C). Therefore, we generated a structure of *Li*Acs1 in complex with ethyl-AMP to assess whether substrate pocket widening also occurs for *Li*Acs1 in a manner that may be consistent with acetoacetate utilization.

The structure of *Li*Acs1 in complex with ethyl-AMP is very similar to the AMP-acetate/CoA bound structure with an RMSD deviation of 1.00 Å between Ca atoms (651 residues). Since the ethyl-AMP structure was obtained without CoA added during crystallization, there's a small shift in the C-terminal domain relative to the CoA bound structure as shown in Supplemental Figure 3A. As previously observed with ethyl-AMP bound ACS structures, the ethyl group of the inhibitor occupies the same site as the acetate molecule (Supplemental Figure 3B). Not surprisingly, the ethyl-AMP inhibitor forms hydrogen bond interactions with D463, T464, Q467, T468, D552 R567 and R578 similar to AMP and the ethyl group is positioned with a hydrophobic pocket formed by I362, T363, V438, T468 and W466 (Supplemental Figure 3C-D). The structure of monoclinic *P* form of the ethyl-AMP complex was also obtained which adopts a nearly identical ligand binding mode. A direct comparison of the ethyl-AMP bound *Li*Acs1 and *Cn*Acs1 illustrates a slightly larger substrate pocket widening for *Li*Acs1 that results from a shift in the CTD (Supplemental Figure 4D-E).

Molecular docking supports acetoacetate utilization by *Li*Acs1.

To assess acetate versus acetoacetate binding energetics, we performed molecular docking experiments for each substrate in the *Li*Acs1 (8SF3) and *Ca*Acs2 (8V4R) structures. Both *Li*Acs1 and *Ca*Acs2 exhibit relatively similar binding energies for acetate, while *Li*Acs1 exhibits a much greater binding energy for acetoacetate (Table 4). The preferred docking pose for acetoacetate in *Li*Acs1 allows binding in a reactive pose (Figure 7C) that is not observed for *Ca*Acs2 (Figure 7D). Therefore, while acetoacetate may be able to bind in the acetate restricted *Ca*Acs2 enzyme albeit with much reduce binding energy compared to *Li*Acs1, the preferred binding orientation is not likely to be reactive.

Discussion

The lack of a separate KBC enzyme encoded by *Leishmania*, despite its reliance on leucine catabolism, has been a puzzling aspect of its metabolism (38). Our demonstration that the *Li*Acs1 has both activities provides an explanation for this metabolic conundrum. Furthermore, the ability of *Li*Acs1 to serve as both an ACS and KBC in *Leishmania infantum* is, to our knowledge, unprecedented for this group of adenylating enzymes. This uniquely described metabolic machinery is highly conserved across *Leishmania* spp. including *L. infantum*, *L. donovani*, *L. braziliensis*, and *L. amazonensis*, but also highly homologous to other Acyl-CoA/NRPS/Luciferase (ANL) family enzymes spanning a broad range of both prokaryotes and eukaryotes. For *Leishmania* it appears this dual functionality suggests a unique evolutionary adaptation, allowing efficient utilization of both acetate and acetoacetate as a product of ketogenesis for energy production and biosynthesis.

To understand how the substrate binding pocket of *Li*Acs1 allows for dual substrate functionality we tested a series of acyl-AMP intermediate mimicking AMP-esters of varying sizes. We observed a more promiscuous substrate binding pocket than either acetate or acetoacetate specific enzymes *Cn*Acs1 or *CnKbc1*. While *Cn*Acs1 primarily accommodates small AMP-esters and *Cn*Kbc1 only accommodates the large butyl-AMP ester, *Li*Acs1 is able to accommodate both small and large AMP-esters. Looking at either the primary sequence homology and or the structural homology of *Li*Acs1 to previously characterized ACSs and KBCs we could not identify an obvious molecular basis that allows for expanded AMP-ester binding or dual ACS/KBC functionality. We attempted to perform a specificity-determining-sites detection strategy utilizing category informed multiple sequence alignment tools: however, we quickly realized that while the annotated pool of ACS and KBC enzymes is quite large the biochemical confirmation of their substrate specificity is sparse. Additionally, given that *Li*Acs1 operates in a newly described third category with ACS/KBC dual functionality it is currently unclear what fraction of annotated ACSs also contain KBC functionality.

There are multiple pieces of data to suggest that *Li*Acs1 substrate specificity may be governed by emergent properties that contribute to overall protein flexibility rather than any specific set of substrate binding residues for this class of enzymes. We already know the CTD flexibility for this class of enzymes is enormous given the dramatic shift between the AD and TE conformations. Overall enzyme and substrate pocket flexibility is likely governed by multiple intramolecular interactions that may include substrate pocket adjacent intramolecular interactions. These interactions can have distal effects to protein stability and substrate accommodation that are not easily discerned. We provide a great example of this in our observation that substrate binding in the AD conformation appears to affect CoA binding in the TE conformation. This became clear as indicated by the difference in CoA substrate inhibition for *Li*Acs1 when either acetate or acetoacetate is supplied. We suspect these complex interactions contribute to *Li*Acs1 exhibiting an expanded substrate pocket flexibility and is supported by an expanded AMP-ester binding profile. This broad substrate accommodation straddles ACS and KBC AMP-ester binding profiles. The most compelling data to suggest substrate pocket flexibility is our observation that a substrate pocket widening occurs in the ethyl-AMP bound state for *Li*Acs1 beyond what we had previously described for *Cn*Acs1 and this substrate pocket widening allows for acetoacetate accommodation. Together, this data supports an overall flexibility of *Li*Acs1 that may contribute to its expanded substrate profile and may also explain why *Li*Acs1 does not form a trimer like *Cn*Acs1 or *Cn*Kbc1. Aside from simply having a larger substrate pocket, acetoacetate accommodation hinges on the acetate binding conformation observed in the *Li*Acs1 structure but not for *Ca*Acs2.

The regulatory mechanisms governing the switch between ACS and KBC activities in *Li*Acs1 remain to be elucidated. It's possible substrate availability alone governs its contribution to overall metabolic flux. Alternatively, our observations of CoA substrate inhibition, particularly its modulation by acetoacetate, hint at a complex regulatory interplay between acid substrate availability, utilization, and CoA sensitivity. This substrate-induced modulation could represent a feedforward mechanism where acetoacetate accumulation relieves CoA inhibition. Conversely, metabolic demands for CoA may increase during a shift from a ketogenic to glycolytic carbon catabolism such that enhanced ACS inhibition is desired.

The unique dual-function of *Li*Acs1 represents a potential target for novel small molecule inhibitors that could, in turn, be selective for *Li*Acs1 over host enzymes given the unique substrate features of *Li*Acs1. By targeting a single enzyme critical for both acetyl-CoA and acetoacetyl-CoA production, it becomes possible to disrupt two essential metabolic pathways simultaneously. Further studies are required to understand the landscape of ACS enzymes that may also serve a dual ACS/KBC role, which may help elucidate the structural and specificity-determining-sites that dictate ACS vs KBC function.

Experimental Procedures

Cloning of Expression Constructs, Expression, and Purification

Full-length *Leishmania infantum* ACS construct (LeinA.00629.b.B1, Uniprot A4I093, 1-705) containing a non-cleavable His tag at the N-terminus (MAHHHHHH) was codon-optimized using ATUM for *E. coli* expression and cloned by ATUM into ATUM vector pD431-SR via SapI cloning, including a double stop after the open reading frame (ORF). An example of the 5′ adapter just prior to ATG is 5′-TACACGTACTTAGTCGCTGAAGCTCTTCT-3′ and the 3′ adapter just after the double stop is 5′-TAGGTACGAACTCGATTGACGGCTCTTCTACC-3′. Codon optimization excluded restriction sites NcoI, NdeI, XhoI, HindIII, and SapI. The pD431-SR vector is kanamycin-resistant with the p15a origin of replication accepting inserts under the T7 promoter with a lac repressor and strong ribosome binding site (RBS). The resulting plasmid was sequence verified and transformed into BL21(DE3) (NEB C2527). An overnight starter culture prepared in LB broth with antibiotic was diluted 1:1000 the following day in LB media also containing antibiotic and grown the OD_{600} between 0.5 and 1.0 where the culture was then cooled to between 18-25 °C. Expression was induced with 1mM isopropyl-β-D thiogalactopyranoside (IPTG) overnight and cell pellets were collected for lysis via sonication as previously described (17, 22). Cleared lysates were subjected to nickel purification and equilibration in overnight dialysis buffer as previously described (17, 22).

Enzyme Activity Detection

Enzyme activity was measured as previously reported for *Cn*Acs1 and *Cn*Kbc1 (17, 22, 39). Briefly, the EnzChek Pyrophosphate assay kit (Thermo) was used as indicated by the manufacturer with the addition of 4 mM $MgCl_2$, 10 mM DTT, and concentrations of CoA, ATP, and acid substrates as indicated with a total reaction volume of 50 μl. The final enzyme concentration of *Li*Acs1 was 3 μg/mL. All reagents were mixed in master mixes as allowed by each assay, aliquoted into 96-well half-well sized plates, incubated for 15 minutes at 37°C, with acid substrate provided as the start reagent. The micro plate was then read continuously in a SpectraMax i3X Multi-Mode plate reader (Molecular Devices) at absorbance 360 nm. Michaelis-Menten constants were determined for each substrate such that the other substrates were provided in excess, except where CoA was provided at concentrations up to the maximum reaction velocity but before substrate inhibition. Kinetic constants (K_m, V_{max}, and K_i) were determined from the non-linear regression of the slopes generated from the linear reaction curves as calculated using the GraphPad Prism statistical software. Hydroxamate forming reactions were performed under the same conditions as the EnzChek with the addition of 150 mM hydroxylamine pH 7.5. The reactions were carried out such that PPi generation was followed as normal to assure reaction curves were stopped within their linear range using trichloroacetate (200 mM) and $FeCl_3$ (370 mM). Absorbance was then measured at 560 nm with background subtracted from no enzyme controls.

Mass Photometry and Dynamic Light Scattering

Mass photometry (MP) experiments were conducted as previously described using a Refeyn TwoMP mass photometer (Refeyn Ltd, Oxford, UK) (40). Briefly, microscope coverslips (24 mm × 50 mm, Thorlabs Inc.) and Silicon gaskets (Grace Bio-Labs) were cleaned by sequential rinsing with Milli-Q water and isopropanol, followed by drying with a filtered air stream. MP measurements were carried out at room temperature in sterile PBS. Calibration of the instrument was performed using a protein standard mixture: β-amylase (Sigma-Aldrich, 56, 112, and 224 kDa) and thyroglobulin (Sigma-Aldrich, 670 kDa). Movies were recorded for 60 seconds (3000 frames) using AcquireMP software (version 2.3.0; Refeyn Ltd) with standard settings. All recorded movies were processed and analyzed using DiscoverMP software (version 2.3.0; Refeyn Ltd). Dynamic light scattering was performed on the same undiluted sample from mass photometry analysis using a DynaPro NanoStar (Wyatt Technology, Santa Barbara, CA) equipped with additional static light scattering detector and temperature control.

Crystallization and Data Collection

Purified *Li*Acs1 was concentrated to 20 mg/mL in 500 mM NaCl, 20 mM Hepes pH 7.5, 5% glycerol, 2 mM DTT, 0.025% sodium azide. All crystallization experiments were setup using an NT8 drop-setting robot (Formulatrix Inc.) and UVXPO MRC (Molecular Dimensions) sitting drop vapor diffusion plates at 18 ºC. 100 nL of protein and 100 nL crystallization solution were dispensed and equilibrated against 50 uL of the latter. Ligand complexes were prepared by adding 2 mM of the AMP, CoA and ethyl-AMP compounds to the protein prior to crystallization. Crystals of *Li*Acs1 were obtained from the following conditions. AMP-Acetate/CoA: Crystal Screen HT (Hampton Research) condition A9 (30% (w/v) PEG 4000, 200 mM ammonium acetate, 100 mM sodium citrate pH 5.6). Samples were vitrified in a fresh drop of crystallant which served as the cryoprotectant. AMP/CoA: JCSG+ E4 (1.26 M ammonium sulfate, 0.2 M lithium sulfate, 100 mM Tris pH 8.5) and cryoprotected in 2.5M Lithium Sulfate. Ethyl-AMP: JCSG+ B4 (10% (w/v) PEG 8000, 8% (v/v) ethylene glycol, 100 mM Hepes pH 7.5) and cryoprotected in 20% PEG 200 + 80% crystallant. AMP-K+/CoA: JCSG+ G10 (30% PEG 2000MME, 150 mM KBr) and cryoprotected in a fresh drop of crystallant. Ethyl-AMP (P21 form): JCSG+ B5 (40% (v/v) MPD, 0.1M Na cacodylate pH 6.5, 5% (w/v) PEG 8000) and cryoprotected in a fresh drop of crystallant. X-ray diffraction data were collected at the National Synchrotron Light Source II (NSLS-II) beamline 19-ID (NYX).

Structure Solution and Refinement

Intensities were integrated using XDS (41) via Autoproc (42) and the Laue class analysis and data scaling were performed with Aimless (43). Structure solution was conducted by molecular replacement with Phaser (44) using previously determined structures of *Cn*ACS1 (PDB 7L4G) and *Salmonella* ACS (PDB 2P2F) for *Li*ACS as the search models. Structure refinement and manual model building were conducted with Phenix (45) and Coot (46) respectively. Structure validation was conducted with Molprobity (47) and figures were prepared using the CCP4MG package (48). Structure superpositions were conducted using GESAMT (49). Crystallographic data are provided in Table 3.

Molecular Docking

Molecular docking of acetate and acetoacetate into ACS enzymes was conducted using the Molecular Operating Environment (MOE, version 2020.01; Chemical Computing Group). The crystal structures of *Li*Acs1 (PDB: 8SF3) and *Ca*Acs2 (PDB: 8V4R) which are bound to both acetate and AMP were used to evaluate substrate preference. Binding energy of acetate was determined via the Londong dG scoring function followed by rescoring using the GBVI/WSA dG function within MOE. Acetoacetate was modeled into the acetate binding site and a global energy minimization was performed using the Amber10:EHT force field. The binding energy of acetoacetate for the ACS structures was evaluated as described above.

Acknowledgments

This work was supported by NIH grants 5R01AI161973 (D.J.K), T32AI007511 (A.J.J) This project has been funded in whole or in part with Federal funds from the National Institute of Allergy and Infectious Diseases, National Institutes of Health, Department of Health and Human Services, under Contract No. 75N93022C00036. This research used resources at the NYX beamline 19-ID, supported by the New York Structural Biology Center, at the National Synchrotron Light Source II, a U.S. Department of Energy (DOE) Office of Science User Facility operated for the DOE Office of Science by Brookhaven National Laboratory under Contract No. DE-SC0012704. The NYX detector instrumentation was supported by grant S10OD030394 through the Office of the Director of the National Institutes of Health. The content is solely the responsibility of the authors and does not necessarily represent the official views of the National Institutes of Health. The purchase of the NMR spectrometer used to obtain results included in this publication was supported by the National Science Foundation under the MRI award CHE-2117776 (T.J.H). The HRMS was supported by the Northern Illinois University Molecular Analysis Core Facility and the National Science Foundation under Grant No. 1726931. The authors would like to thank Dr. Zhen Xu and Dr. Nicholas Schnicker of the University of Iowa Protein and Crystallography Facility for their assistance and training in mass photometry.

Data Availability

The coordinates and structure factors for the *Li*Acs1 and *Ca*Acs2 structures were deposited to the Worldwide Protein Databank (wwPDB) with the accession codes 8V4R, 8SF3, 8U2T, 8U2R, 8U2U, and 8U2S as indicated in Table 3. All other data is presented in the manuscript.

References

1. Alvar J, et al. (2012) Leishmaniasis worldwide and global estimates of its incidence. *PLoS One* 7(5):e35671.

2. Grifferty G, et al. (2021) Vulnerabilities to and the Socioeconomic and Psychosocial Impacts of the Leishmaniases: A Review. *Res Rep Trop Med*:135–151.

3. Torres-Guerrero E, Quintanilla-Cedillo MR, Ruiz-Esmenjaud J, Arenas R (2017) Leishmaniasis: a review. *F1000Research* 6.

4. Hefnawy A, Berg M, Dujardin J-C, De Muylder G (2017) Exploiting knowledge on Leishmania drug resistance to support the quest for new drugs. *Trends Parasitol* 33(3):162–174.

5. Picado A, Dash AP, Bhattacharya S, Boelaert M (2012) Vector control interventions for visceral leishmaniasis elimination initiative in South Asia, 2005-2010. *Indian J Med Res* 136(1):22–31.

6. Teixeira DE, et al. (2013) The cell biology of Leishmania: how to teach using animations. *PLoS Pathog* 9(10):e1003594.

7. Naderer T, McConville MJ (2008) The Leishmania–macrophage interaction: a metabolic perspective. *Cell Microbiol* 10(2):301–308.

8. McConville MJ, Naderer T (2011) Metabolic pathways required for the intracellular survival of Leishmania. *Annu Rev Microbiol* 6:543–561.

9. McConville MJ, De Souza D, Saunders E, Likic VA, Naderer T (2007) Living in a phagolysosome; metabolism of Leishmania amastigotes. *Trends Parasitol* 23(8):368–375.

10. Opperdoes FR, Coombs GH (2007) Metabolism of Leishmania: proven and predicted. *Trends Parasitol* 23(4):149–158.

11. Millerioux Y, et al. (2018) De novo biosynthesis of sterols and fatty acids in the Trypanosoma brucei procyclic form: Carbon source preferences and metabolic flux

redistributions. *PLoS Pathog* 14(5):e1007116.

12. Zhou W, Cross GAM, Nes WD (2007) Cholesterol import fails to prevent catalyst-based inhibition of ergosterol synthesis and cell proliferation of Trypanosoma brucei. *J Lipid Res* 48(3):665–673.

13. Guerra B, et al. (2021) The mevalonate pathway, a metabolic target in cancer therapy. *Front Oncol* 11:626971.

14. Soumya N, Panara MN, Neerupudi KB, Singh S (2017) Functional analysis of an AMP forming acetyl CoA synthetase from Leishmania donovani by gene overexpression and targeted gene disruption approaches. *Parasitol Int* 66(1):992–1002.

15. Ohgami M, Takahashi N, Yamasaki M, Fukui T (2003) Expression of acetoacetyl-CoA synthetase, a novel cytosolic ketone body-utilizing enzyme, in human brain. *Biochem Pharmacol* 65(6):989–994.

16. Hasegawa S, et al. (2012) Acetoacetyl-CoA synthetase, a ketone body-utilizing enzyme, is controlled by SREBP-2 and affects serum cholesterol levels. *Mol Genet Metab* 107(3):553–560.

17. Alden KM, Jezewski AJ, Beattie SR, Fox III D, Krysan DJ (2022) Genetic interaction analysis reveals that Cryptococcus neoformans utilizes multiple acetyl-CoA-generating pathways during infection. *MBio*:e01279-22.

18. Mitchell CA, Tucker AC, Escalante-Semerena JC, Gulick AM (2015) The structure of S. lividans acetoacetyl-C o A synthetase shows a novel interaction between the C-terminal extension and the N-terminal domain. *Proteins Struct Funct Bioinforma* 83(3):575–581.

19. Vögeli B, et al. (2018) Archaeal acetoacetyl-CoA thiolase/HMG-CoA synthase complex channels the intermediate via a fused CoA-binding site. *Proc Natl Acad Sci* 115(13):3380–3385.

20. Van Den Berg MA, Steensma HY (1995) ACS2, a Saccharomyces cerevisiae gene encoding acetyl-coenzyme A synthetase, essential for growth on glucose. *Eur J Biochem*

231(3):704–713.

21. De Virgilio C, et al. (1992) Cloning and disruption of a gene required for growth on acetate but not on ethanol: The acetyl-coenzyme a synthetase gene of Saccharmoyces cerevisiae. *Yeast* 8(12):1043–1051.

22. Jezewski AJ, et al. (2021) Structural Characterization of the Reaction and Substrate Specificity Mechanisms of Pathogenic Fungal Acetyl-CoA Synthetases. *ACS Chem Biol* 16(8):1587–1599.

23. Luong A, Hannah VC, Brown MS, Goldstein JL (2000) Molecular characterization of human acetyl-CoA synthetase, an enzyme regulated by sterol regulatory element-binding proteins. *J Biol Chem* 275(34):26458–26466.

24. Sievers F, et al. (2011) Fast, scalable generation of high-quality protein multiple sequence alignments using Clustal Omega. *Mol Syst Biol* 7(1):539.

25. Sievers F, Higgins DG (2018) Clustal Omega for making accurate alignments of many protein sequences. *Protein Sci* 27(1):135–145.

26. Sievers F, Barton GJ, Higgins DG (2020) Multiple sequence alignments. *Bioinformatics* 227:227–250.

27. Madeira F, et al. (2024) The EMBL-EBI Job Dispatcher sequence analysis tools framework in 2024. *Nucleic Acids Res*:gkae241.

28. Manandhar M, Cronan JE (2013) Proofreading of noncognate acyl adenylates by an acyl-coenzyme a ligase. *Chem Biol* 20(12):1441–1446.

29. Berg P (1956) Acyl adenylates: an enzymatic mechanism of acetate activation. *J Biol Chem* 222(2):991–1013.

30. Wilson DJ, Aldrich CC (2010) A continuous kinetic assay for adenylation enzyme activity and inhibition. *Anal Biochem* 404(1):56–63.

31. Farrar WW, Plowman KM (1975) Kinetics of acetyl-CoA synthetase—I. Mode of addition of substrates. *Int J Biochem* 6(8):537–542.

32. Gulick AM (2009) Conformational dynamics in the Acyl-CoA synthetases, adenylation domains of non-ribosomal peptide synthetases, and firefly luciferase. *ACS Chem Biol* 4(10):811–827.

33. Lu X, Zhang H, Tonge PJ, Tan DS (2008) Mechanism-based inhibitors of MenE, an acyl-CoA synthetase involved in bacterial menaquinone biosynthesis. *Bioorg Med Chem Lett* 18(22):5963–5966.

34. Gupte A, et al. (2008) Inhibition of siderophore biosynthesis by 2-triazole substituted analogues of 5′-O-[N-(salicyl) sulfamoyl] adenosine: antibacterial nucleosides effective against Mycobacterium tuberculosis. *J Med Chem* 51(23):7495–7507.

35. Lux MC, Standke LC, Tan DS (2019) Targeting adenylate-forming enzymes with designed sulfonyladenosine inhibitors. *J Antibiot (Tokyo)* 72(6):325–349.

36. Yung-Chi C, Prusoff WH (1973) Relationship between the inhibition constant (KI) and the concentration of inhibitor which causes 50 per cent inhibition (I50) of an enzymatic reaction. *Biochem Pharmacol* 22(23):3099–3108.

37. Ingram-Smith C, Woods BI, Smith KS (2006) Characterization of the acyl substrate binding pocket of acetyl-CoA synthetase. *Biochemistry* 45(38):11482–11490.

38. Blum JJ (1991) Oxidation of leucine by Leishmania donovani. *J Protozool* 38(6):527–531.

39. Comerford SA, et al. (2014) Acetate dependence of tumors. *Cell* 159(7):1591–1602.

40. Schnicker NJ, Xu Z, Amir M, Gakhar L, Huang C-L (2024) Conformational landscape of soluble α-klotho revealed by cryogenic electron microscopy. *bioRxiv*.

41. Kabsch W (1988) Automatic indexing of rotation diffraction patterns. *J Appl Crystallogr* 21(1):67–72.

42. Vonrhein C, et al. (2011) Data processing and analysis with the autoPROC toolbox. *Acta Crystallogr Sect D Biol Crystallogr* 67(4):293–302.

43. Evans PR (2011) An introduction to data reduction: space-group determination, scaling and intensity statistics. *Acta Crystallogr Sect D Biol Crystallogr* 67(4):282–292.

44. McCoy AJ, et al. (2007) Phaser crystallographic software. *J Appl Crystallogr* 40(4):658–674.

45. Adams PD, et al. (2010) PHENIX: a comprehensive Python-based system for macromolecular structure solution. *Acta Crystallogr Sect D Biol Crystallogr* 66(2):213–221.

46. Lohkamp B, Scott WG, Cowtan K (2010) Features and development of Coot. *Acta Crystallogr Sect D Biol Crystallogr* 66(Pt 4).

47. Chen VB, et al. (2010) MolProbity: all-atom structure validation for macromolecular crystallography. *Acta Crystallogr Sect D Biol Crystallogr* 66(1):12–21.

48. Potterton L, et al. (2004) Developments in the CCP4 molecular-graphics project. *Acta Crystallogr Sect D Biol Crystallogr* 60(12):2288–2294.

49. Krissinel E (2012) Enhanced fold recognition using efficient short fragment clustering. *J Mol Biochem* 1(2):76.

50. Evans PR. An introduction to data reduction: space-group determination, scaling and intensity statistics. *Acta Crystallogr. Sect. D Biol. Crystallogr*. 2011;67(4):282–92.

51. Evans P. Scaling and assessment of data quality. Vol. 62, *Acta crystallogr*. [Copenhagen, Denmark] :; 2006. p. 72–82.

52. Diederichs K, Karplus PA. Improved R-factors for diffraction data analysis in macromolecular crystallography. Vol. 4, Nature structural biology. New York, N.Y. :; 1997. p. 269–75.

53. Weiss MS. Global indicators of X-ray data quality. Vol. 34, Journal of applied crystallography. Oxford, England :; 2001. p. 130.

54. Karplus PA, Diederichs K. Linking Crystallographic Model and Data Quality. Science (80). 2012;336(6084):1030–3.

55. Evans P. Biochemistry. Resolving some old problems in protein crystallography. Science (80). 2012;336(6084):986–7.

Figure Legends

Figure 1. Route of acetoacetate utilization by *Leishmania* is not obvious based on encoded CoA ligase homology. (A) Schematic illustrating leucine catabolism and its end products of acetoacetate and acetyl-CoA. (B) CoA ligases encoded by *Leishmania* spp. and their homology to verified ACS and KBC functioning enzymes. The following are identified by their corresponding uniprot ID: *Cryptococcus neoformans* Acs1 (*Cn*Acs1: J9VFT1), *Saccharomyces cerevisiae* Acs2 (*Sc*Acs2: P52910), *Saccharomyces cerevisiae* Acs1 (*Sc*Acs1: Q01574), *Streptomyces lividans* Acs1 (*Sl*Acs1: A0A7U9HBW6), *Homo sapiens* Acss2 (*Hs*Acss2: Q9NR19), *Leishmania braziliensis* Acs1 (*Lb*Acs1: A4HCR9), *Leishmania braziliensis* Acs2 (*Lb*Acs2: A4HCU1), *Leishmania infantum* Acs1 (*Li*Acs1: A4I093), *Leishmania infantum* Acs2 (*Li*Acs2: A4I0C2), *Leishmania donovani* Acs1 (*Ld*Acs1: E9BG78), *Leishmania donovani* Acs2 (*Ld*Acs2: A0A3S7WXN0), *Cryptococcus neoformans* Kbc1 (*Cn*Kbc,: J9VT24), *Homo sapiens* Aacs (*Hs*Aacs: Q86V21), *Streptomyces lividans* Aacs (*Sl*Aacs: A0A7U9DRD6). *Leishmania amazonensis* Acs1 (*La*Acs1: LAMA_000440100.1) is identified by its EuPathDB ID and with a modified reading frame as discussed in the text.

Figure 2. *Li*ACS exists as a monomer in solution. Recombinantly expressed *Li*Acs1, *Cn*Acs1, and *Cn*Kbc1 are pure as indicated by both SDS-PAGE and form a uniform population of monomers in the case of *Li*Acs1 (A) and trimers in the case of *Cn*Acs1 (B) and *Cn*Kbc1 (C) as indicated by single particle analysis via mass photometry.

Figure 3. *Li*Acs1 is active and exhibits acetoacetate and acetate substrate utilization. (A) Dilution series indicates enzyme is highly active across a long linear range with respect to detection assay. (B) pH sensitivity of *Li*Acs1 as normalized to pH 6. (C) Substrate utilization of *Li*Acs1.

Figure 4. Enzyme kinetics of *Li*Acs1. Representative K_m curves for (A) ATP, (B) acetate, (C) acetoacetate, and (D) CoA. K_m curves for CoA were performed with either acetate or acetoacetate provided as co-substrate. All curves were fit using the GraphPad prism statistical software and K_m's were calculated from a minimum of three experimental replicates as reported in text.

Figure 5. Visual comparison of AMP-ester inhibition profile according to Van der Waals volume. Inverse log of inhibition data from Table 1 plotted according to increasing Van der Waals volume from left to right.

Figure 6. Structure of *Li*Acs1. (A) *Cn*Acs1 (magenta) superimposed with *Li*Acs1 (coral). The ligands from Leishmania ACS are colored: AMP (cyan), acetate (gray) and CoA (yellow). (B) Hydrogen bonds between *Li*Acs1 and CoA (yellow), AMP (cyan) and acetate (gray). (C-D) Electron density (Fo-Fc, 3s) for acetate/AMP and CoA respectively.

Figure 7. *Li*Acs1 substrate pocket size allows viable pose of docked acetoacetate. Substrate pocket size differences illustrated by distance from conserved tryptophan wall to phosphate of AMP for *Li*Acs1 8SF3 (coral) (A) and *Ca*Acs2 8V4R (blue) (B). Structures were oriented to illustrate the maximal distance measured without acid substrate present. Molecular docking was performed and acetoacetate was modeled into the acetate substrate pocket for *Li*Acs1 (8SF3) (C) and *Ca*Acs2 (8V4R) (D). Structures were oriented to illustrate the alternative binding poses of acetoacetate that were adopted when performing a global energy minimization using the Amber10:EHT force field in Molecular Operating Environment (MOE, version 2020.01; Chemical Computing Group). In all panels, only residues within 4 angstroms of the crystalized acetate ligand that comprised the acid substrate pocket were illustrated. Illustrations rendered by Pymol.

Table 1. Dynamic light scattering data for recombinant proteins.

Table 2. Inhibition profile of AMP-ester isosteres.

Table 3. Crystallographic data for *Li*ACS structures.

Table 4. Molecular docking of acetate vs acetoacetate.

Figure 1

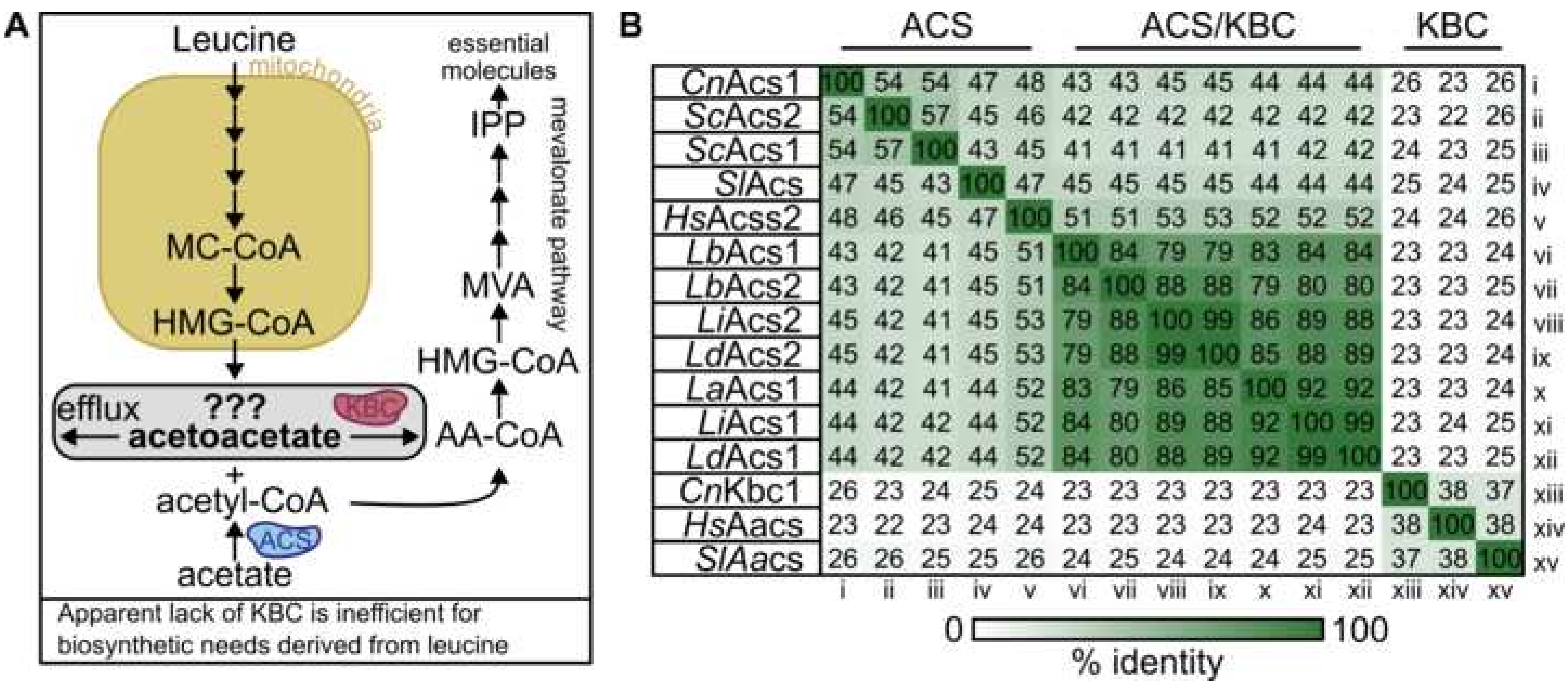
A
Leucine
mitochondria
MC-CoA
HMG-CoA
efflux ???
acetoacetate
KBC
+
acetyl-CoA
ACS
acetate
essential molecules
IPP
MVA
HMG-CoA
AA-CoA
mevalonate pathway
Apparent lack of KBC is inefficient for biosynthetic needs derived from leucine
B
ACS
ACS/KBC
KBC
CnAcs1 100 54 54 47 48 43 43 45 45 44 44 44 26 23 26 i
ScAcs2 54 100 57 45 46 42 42 42 42 42 42 42 23 22 26 ii
ScAcs1 54 57 100 43 45 41 41 41 41 41 42 42 24 23 25 iii
SlAcs 47 45 43 100 47 45 45 45 45 44 44 44 25 24 25 iv
HsAcss2 48 46 45 47 100 51 51 53 53 52 52 52 24 24 26 v
LbAcs1 43 42 41 45 51 100 84 79 79 83 84 84 23 23 24 vi
LbAcs2 43 42 41 45 51 84 100 88 88 79 80 80 23 23 25 vii
LiAcs2 45 42 41 45 53 79 88 100 99 86 89 88 23 23 24 viii
LdAcs2 45 42 41 45 53 79 88 99 100 85 88 89 23 23 24 ix
LaAcs1 44 42 41 44 52 83 79 86 85 100 92 92 23 23 24 x
LiAcs1 44 42 42 44 52 84 80 89 88 92 100 99 23 24 25 xi
LdAcs1 44 42 42 44 52 84 80 88 89 92 99 100 23 23 25 xii
CnKbc1 26 23 24 25 24 23 23 23 23 23 23 23 100 38 37 xiii
HsAacs 23 22 23 24 24 23 23 23 23 23 24 23 38 100 38 xiv
SlAacs 26 26 25 25 26 24 25 24 24 24 25 25 37 38 100 xv
i ii iii iv v vi vii viii ix x xi xii xiii xiv xv
0
100
% identity

Figure 2

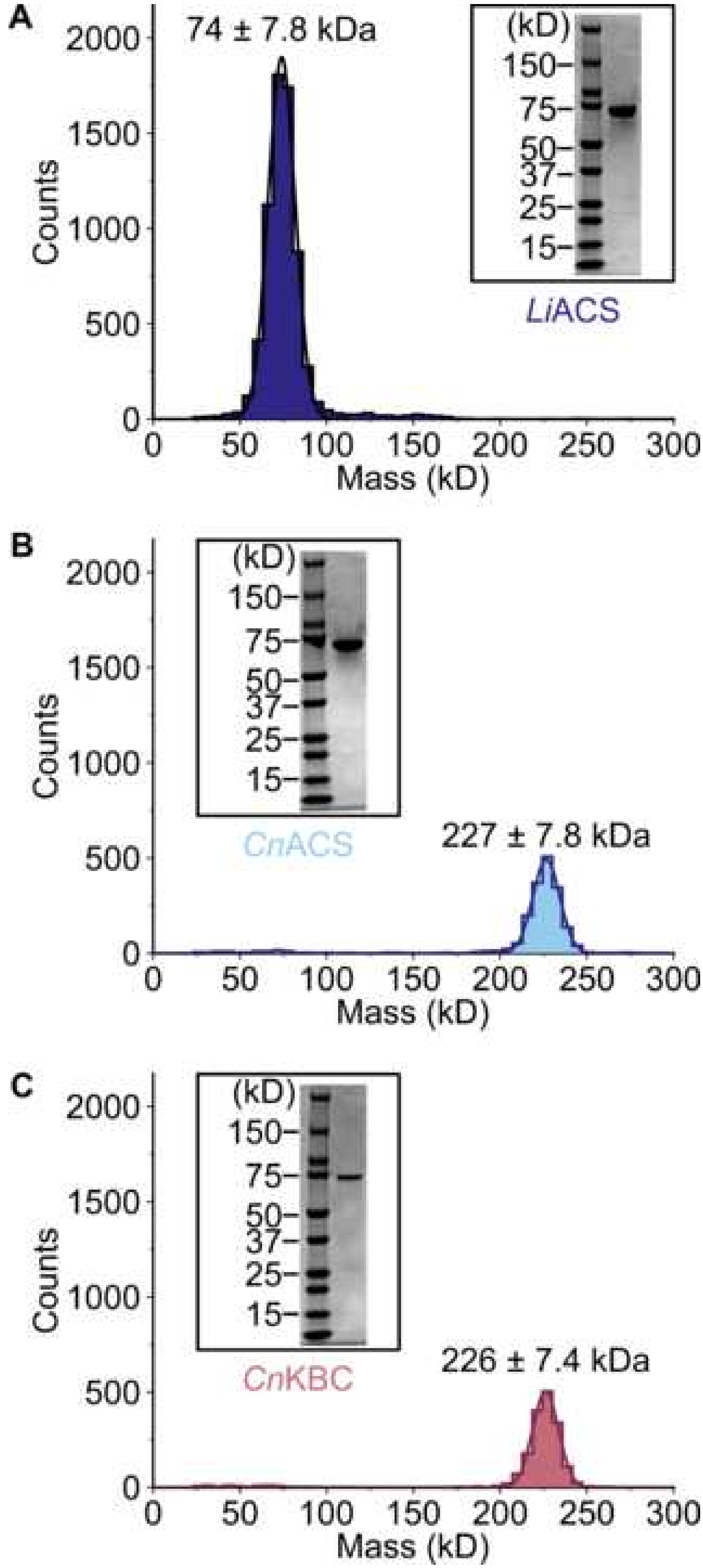
A
74 ± 7.8 kDa
(kD)
150
75
50
37
25
15
LiACS
Counts
0
500
1000
1500
2000
0
50
100
150
200
250
300
Mass (kD)
B
(kD)
150
75
50
37
25
15
CnACS
227 ± 7.8 kDa
Counts
Mass (kD)
C
(kD)
150
75
50
37
25
15
CnKBC
226 ± 7.4 kDa
Counts
Mass (kD)

Figure 3

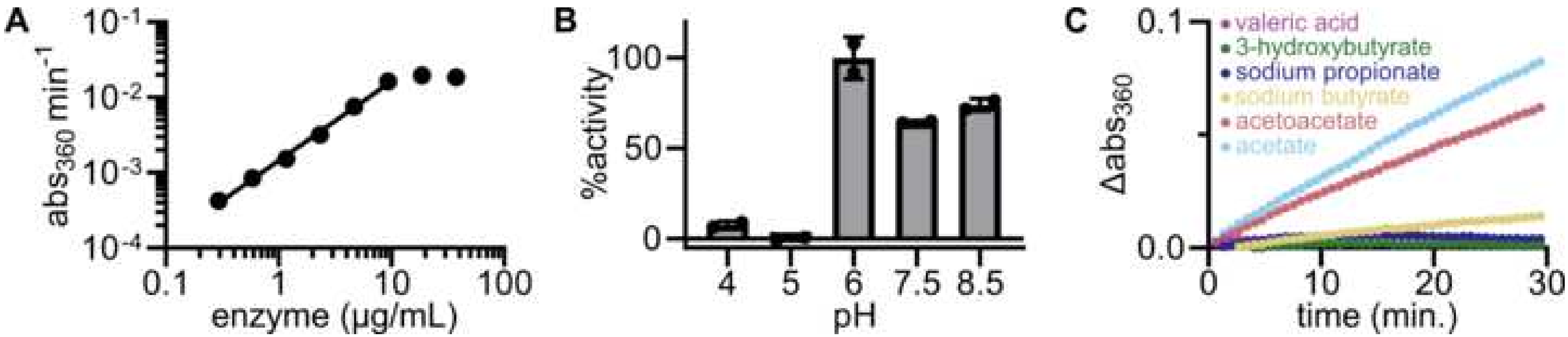
A
10-1
10-2
10-3
10-4
abs360 min-1
0.1
1
10
100
enzyme (µg/mL)
B
100
50
0
%activity
4
5
6
7.5
8.5
pH
C
0.1
0.0
Δabs360
valeric acid
3-hydroxybutyrate
sodium propionate
sodium butyrate
acetoacetate
acetate
0
10
20
30
time (min.)

Figure 4

Click here to access/download;Main Figure (High Resolution);Figure 4.png

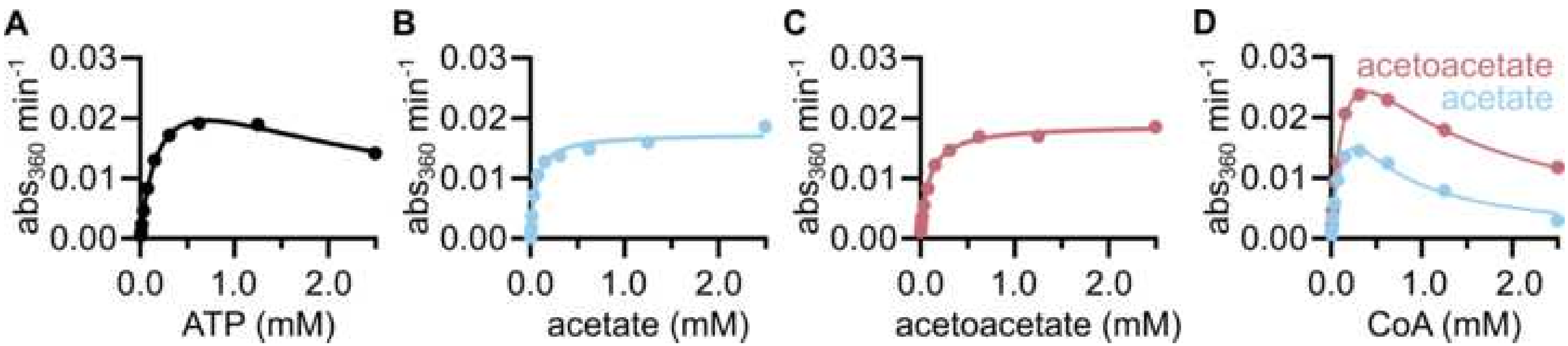

Figure 5

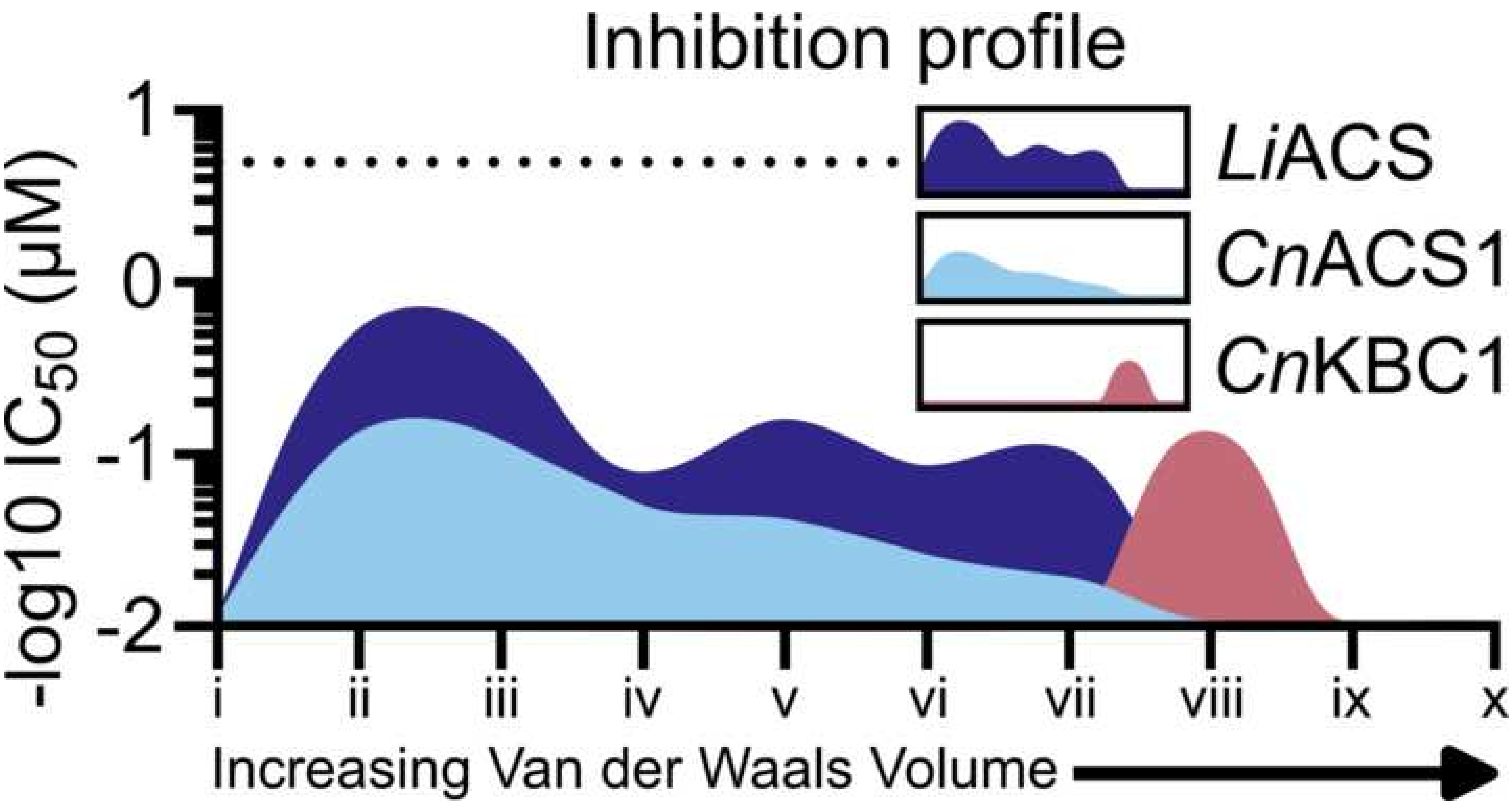

Inhibition profile
-log10 IC50 (μM)
1
0
-1
-2
LiACS
CnACS1
CnKBC1
i
ii
iii
iv
v
vi
vii
viii
ix
x
Increasing Van der Waals Volume

Figure 6

Click here to access/download;Main Figure (High Resolution);Figure 6.png

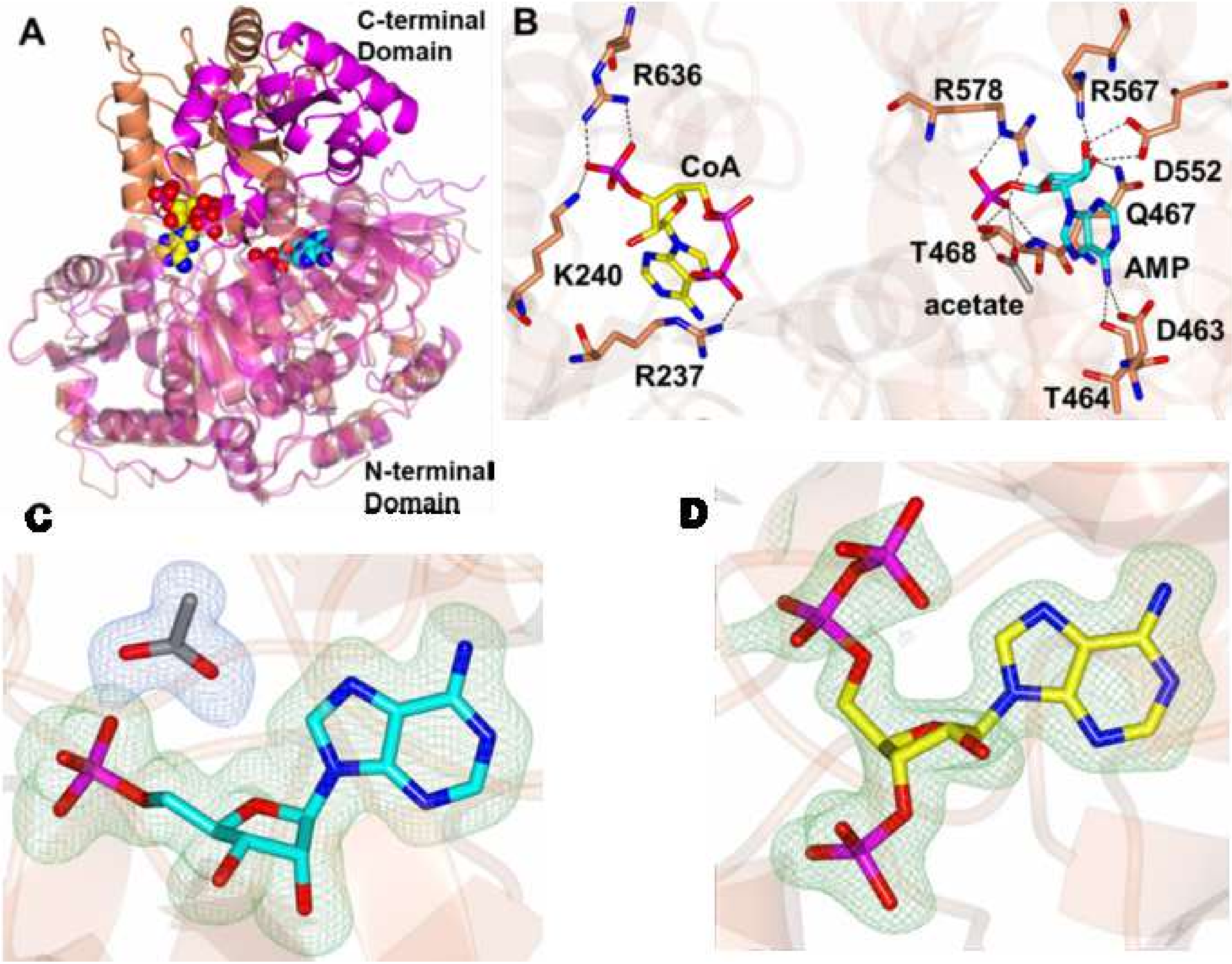

Figure 7 Click here to access/download;Main Figure (High Resolution);Figure 7.png

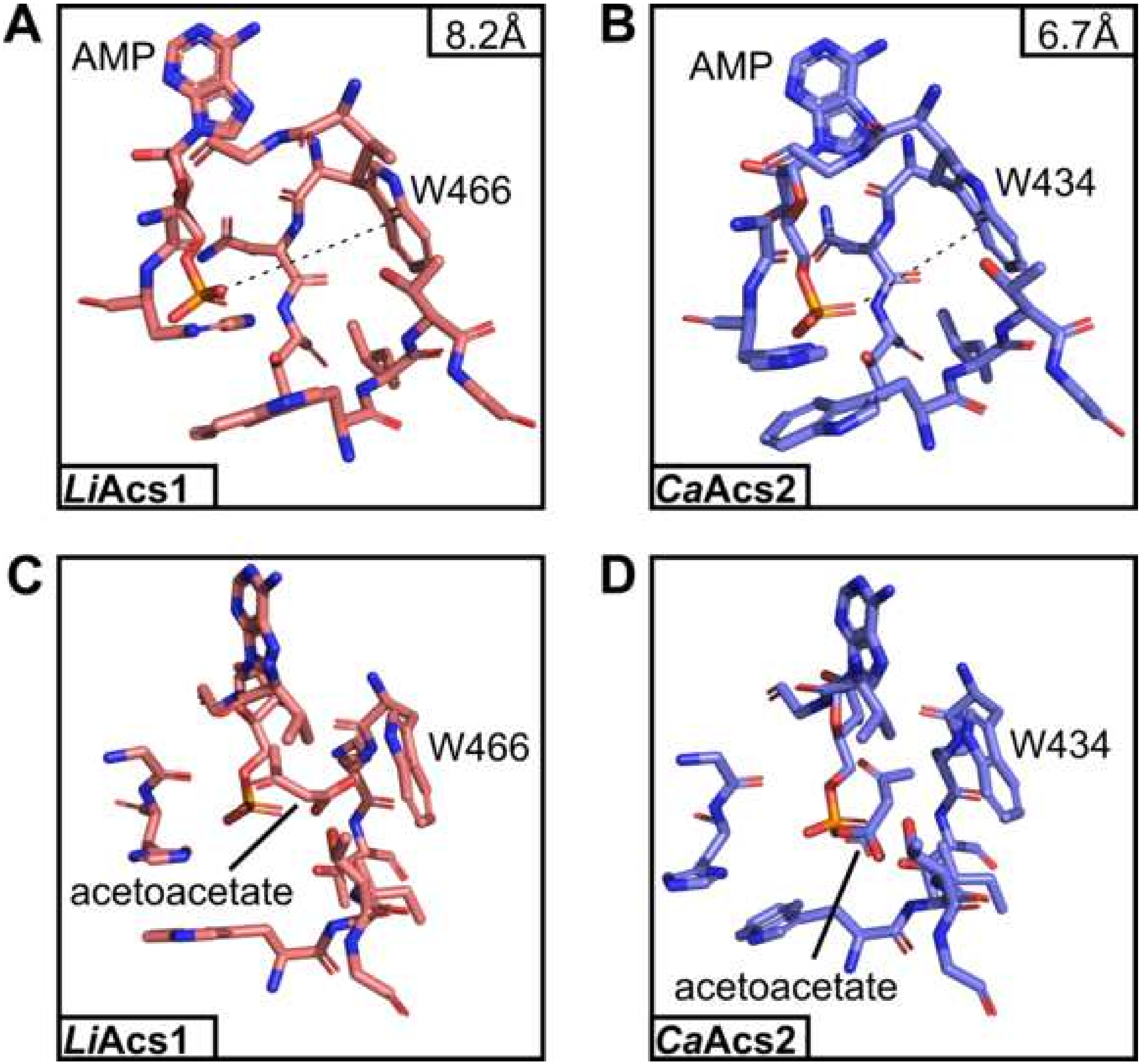

			Range 1 (0.1-20 nm)		
	radius (nm)	Mw-R (kDa)	radius (nm)	Mw-R (kDa)	% mass
***Li*ACS**	3.69 ± 0.06	71.5 ± 1.7	4.12 ± 0.10	92.3 ± 5.1	100.0
***Cn*ACS**	9.84 ± 1.21	724 ± 208	6.43 ± 0.30	262 ± 28	98.9 ± 0.6
***Cn*KBC**	6.79 ± 0.06	296 ± 5.2	5.98 ± 0.66	225 ± 64	99.8 ± 0.1

Table 1. Dynamic light scattering data for recombinant proteins.

#	compound	*Cn*Acs1		*Cn*Kbc1		*Li*Acs1	
		IC_{50} (μM)	95% CI [LL, UL]	IC_{50} (μM)	95% CI [LL, UL]	IC_{50} (μM)	95% CI [LL, UL]
i	methyl-AMP	>100		>100		69.9	[52.8, 98.9]
ii	ethyl-AMP	8.0	[5.8, 11.1]	>100		2.0	[1.4, 2.8]
iii	cyclopropyl-AMP	8.7	[7.5, 10.2]	>100		2.2	[1.8, 2.7]
iv	propyl-AMP	21.1	[11.3, 48.0]	>100		13.5	[10.7, 17.0]
v	isopropyl-AMP	25.3	[21.6, 29.6]	>100		6.7	[5.5, 8.3]
vi	allyl-AMP	41.0	[30.0, 59.8]	>100		12.5	[10.6, 14.8]
vii	propargyl-AMP	55.1	[48.8, 62.6]	>100		10.2	[7.5, 13.9]
viii	butyl-AMP	>100		7.8	[5.7, 10.8]	>100	
ix	diethyl-AMP	>100		>100		>100	
x	cyclopentyl-AMP	>100		>100		>100	

Table 2. Inhibition profile of AMP-ester isosteres.

Sample **Ligand** **PDB Code**	***Li*Acs1** **AMP-Acetate/CoA** **(8SF3)**	***Li*Acs1** **AMP/CoA** **(8U2T)**	***Li*Acs1** **Ethyl-AMP** **(8U2R)**	***Li*Acs1** **AMP-K+/CoA** **(8U2U)**	***Li*Acs1** **Ethyl-AMP-P21** **(8U2S)**	***Ca*Acs2** **Amp-CoA** **(8V4R)**
Data Collection						
Unit-cell parameters (Å, °)	*a*=59.02 *b*=69.38 *c*=151.62	*a*=59.07 *b*=69.92 *c*=150.72	*a*=58.91 *b*=74.15 *c*=151.05	*a*=58.75 *b*=69.46 *c*=149.38	*a*=91.21 *b*=61.81 *c*=134.81 *b*=92.98	*a*=*b*=139.41 *c*=542.25
Space group	$P2_12_12_1$	$P2_12_12_1$	$P2_12_12_1$	$P2_12_12_1$	$P2_1$	$P6_122$
Resolution (Å)[1]	151.62-1.70 (1.74-1.70)	49.49-1.65 (1.68-1.65)	46.45-1.55 (1.58-1.55)	74.69-1.97 (2.02-1.97)	134.63-2.52 (2.59-2.52)	49.46-2.70 (2.75-2.70)
Wavelength (Å)	0.9795	0.9795	0.9795	0.9795	0.9795	0.9795
Temperature (K)	100	100	100	100	100	100
Observed reflections	898,647	1,022,350	1,288,859	583,642	272,635	1,734,018
Unique reflections	68,961	75,992	96,781	44,111	51,168	86,857
<I/□(I)>[1]	12.3 (1.8)	14.5 (1.9)	16.0 (1.8)	13.5 (1.6)	9.3 (1.6)	14.5 (1.7)
Completeness (%)[1]	99.5 (98.5)	100 (100)	100 (100)	99.9 (99.6)	99.9 (100)	100 (100)
Multiplicity[1]	13.0 (13.6)	13.5 (13.9)	13.3 (13.6)	7.0 (6.4)	5.3 (5.6)	20.0 (19.1)
R_{merge} (%)[1, 2]	12.8 (175.0)	11.0 (173.1)	8.4 (164.2)	11.2 (161.4)	13.7 (118.0)	18.5 (235.2)
R_{meas} (%)[1, 4]	13.3 (181.7)	11.5 (179.7)	8.7 (170.6)	11.7 (168.7)	15.2 (129.9)	18.9 (241.6)
R_{pim} (%)[1, 4]	3.7 (48.8)	3.1 (47.8)	2.4 (46.0)	3.2 (47.5)	6.4 (53.7)	4.2 (55.1)
$CC_{1/2}$ [1, 5]	0.998 (0.693)	0.999 (0.762)	0.999 (0.654)	0.999 (0.873)	0.997 (0.596)	0.999 (0.800)
Refinement						
Resolution (Å) [1]	44.95-1.70	45.12-1.65	23.84-1.55	40.47-1.97	91.08-2.52	49.46-2.70
Reflections (working/test)[1]	65,452/3,405	72,074/3,795	91,862/4,819	64,534/2,196	48,521/2,575	82,259/4,353
R_{factor} / R_{free} (%)[1,3]	15.0/18.7	15.4/18.2	15.1/17.4	16.3/21.6	18.6/21.9	20.6/23.1
No. of atoms (Protein/Ligands/ Water)	5,248/58/462	5,196/54/476	5,210/25/503	5,192/54/222	10,161/50/17	14,387/195/41
Model Quality						
R.m.s deviations						
Bond lengths (Å)	0.009	0.009	0.008	0.012	0.002	0.003
Bond angles (°)	1.012	0.997	0.942	1.008	0.505	0.617
Mean *B*-factor (Å^2)						
All Atoms	25.8	27.1	31.8	45.1	58.7	82.4
Protein	25.1	26.2	31.2	45.1	58.6	82.1
Ligand	27.6	32.1	20.9	44.8	41.6	106.6
Water	33.0	34.4	38.0	44.9	48.8	56.5
Coordinate error (maximum likelihood) (Å)	0.19	0.17	0.14	0.19	0.30	0.35
Ramachandran Plot						
Most favored (%)	97.6	97.6	97.1	97.9	96.1	95.6
Additionally allowed (%)	2.4	2.4	2.9	2.0	3.9	3.2

1) Values in parenthesis are for the highest resolution shell.
2) $R_{merge} = \sum_{hkl}\sum_i |I_i(hkl) - \langle I(hkl)\rangle| / \sum_{hkl}\sum_i I_i(hkl)$, where $I_i(hkl)$ is the intensity measured for the *i*th reflection and $\langle I(hkl)\rangle$ is the average intensity of all reflections with indices hkl.
3) $R_{factor} = \sum_{hkl} ||F_{obs}(hkl)| - |F_{calc}(hkl)|| / \sum_{hkl} |F_{obs}(hkl)|$; Rfree is calculated in an identical manner using 5% of randomly selected reflections that were not included in the refinement.
4) R_{meas} = redundancy-independent (multiplicity-weighted) R_{merge} (50, 51). R_{pim} = precision-indicating (multiplicity-weighted) R_{merge} (52, 53).
5) $CC_{1/2}$ is the correlation coefficient of the mean intensities between two random half-sets of data (54, 55).

Table 3. Crystallographic data for *Li*Acs1 and *Ca*Acs2 structures.

ligand	***Ca*Acs2** (8V4R) (ΔG -kcal/mol)	***Li*Acs1** (8SF3) (ΔG -kcal/mol)
acetate	-3.95	-3.86
acetoacetate	-3.65	-4.90

Table 4. Molecular docking of acetate vs acetoacetate.

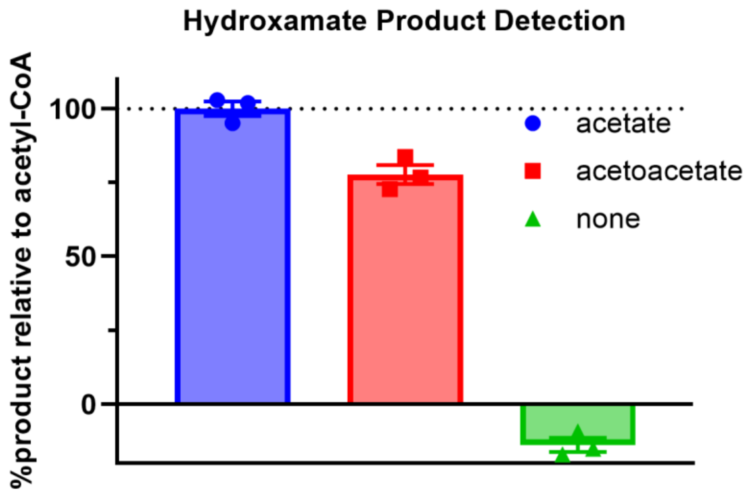

Supplemental Figure 1. Acyl-CoA product detection. Acyl-CoA product formation is confirmed in the presence of acetate and acetoacetate by measuring hydroxamate product formation in the presence of hydroxylamine and iron.

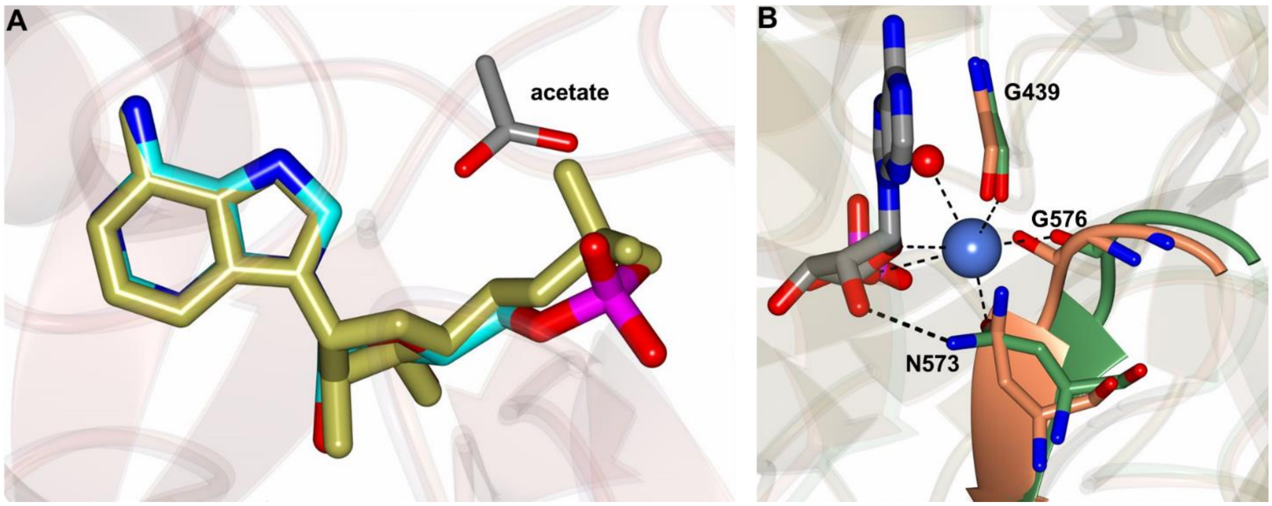

Supplemental Figure 2. Superposition of *Li*Acs1 structures (A) Acetate (cyan) and non-acetate (gold) bound structures showing the binding mode of the AMP molecules. (B) Comparison of the acetate (coral) and potassium bound (green) *Li*Acs1 structures. Binding of a potassium ion (blue sphere) near the AMP molecule results in a slight shift in the loop containing G576 and N573 which forms a new contact with the AMP ligand.

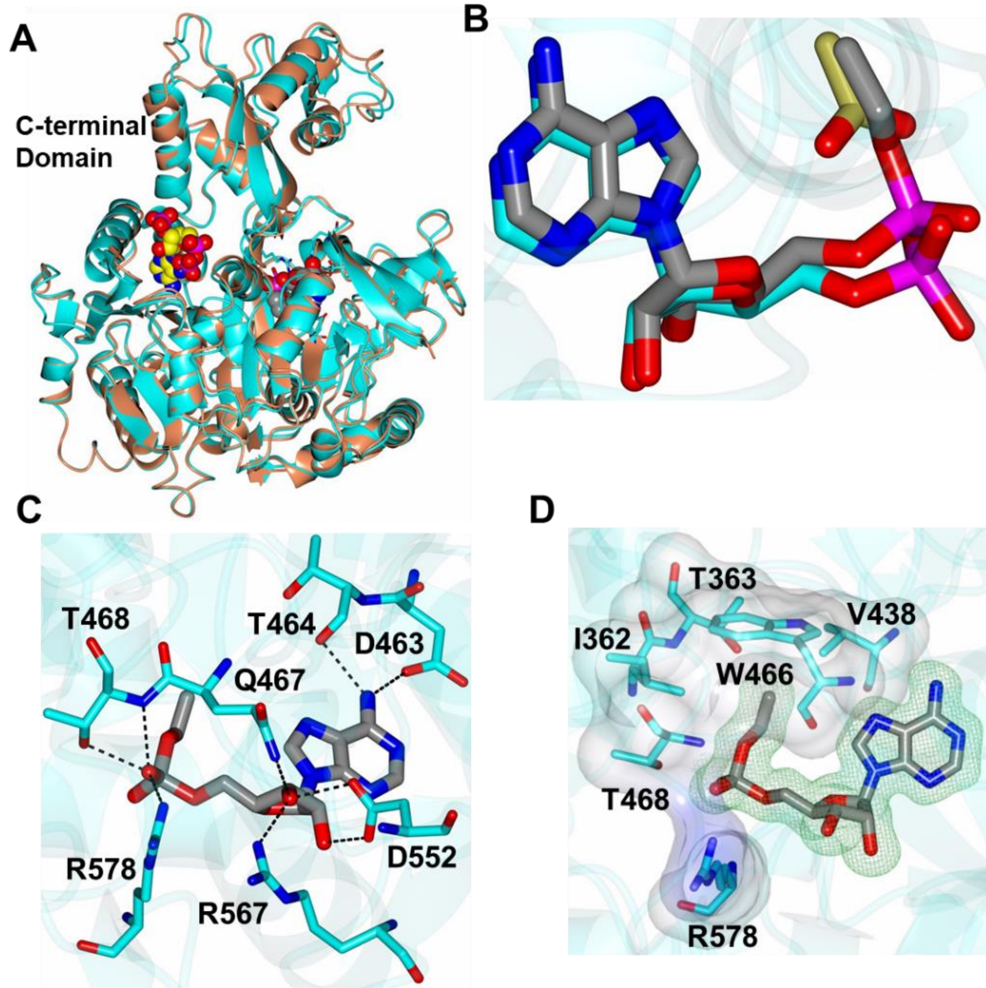

Supplemental Figure 3. Structure of *Li*Acs1 in complex with ethyl-AMP. (A) Superposition of the ethyl-AMP structure (cyan) with the AMP-acetate/CoA complex (coral). The CoA and ethyl-AMP molecule are drawn as yellow and gray spheres respectively. (B) Position of the acetate molecule (gold) relative to ethyl-AMP in the superimposed structures. (C) Hydrogen bond interactions (dashed lines) to the ethyl-AMP molecule (gray). (D) Electron density (Fo-Fc, 3s, green mesh) for the ethyl-AMP molecule. The ethyl group is positioned in a hydrophobic cleft depicted by the transparent electrostatic surface.

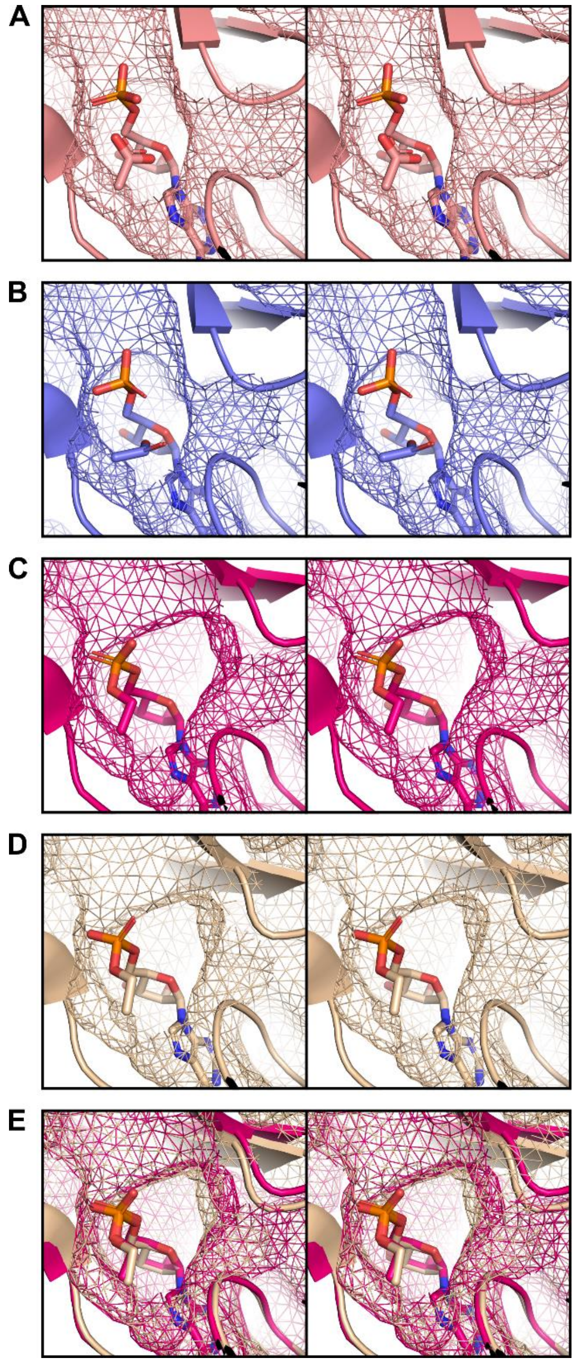

Supplemental Figure 4. *Li*Acs1 exhibits alternative acetate binding and increased pocket flexibility. Stereo images of (A) AMP, acetate binding pocket for *Li*Acs1, (B) AMP, acetate binding pocket for *Ca*Acs2, (C) ethyl-AMP bound *Li*Acs1, (D) ethyl-AMP bound *Ca*Acs2, and the superposition of C & D (E).

Author CRediT Statement

Andrew J. Jezewski: Conceptualization, Methodology, Validation, Formal analysis, Investigation, Data Curation, Writing - Original Draft, Writing - Review & Editing, Visualization **Taiwo E. Esan**: Conceptualization, Methodology, Validation, Formal analysis, Investigation, Data Curation **Andrew J. Fuller**: Conceptualization, Methodology, Validation, Formal analysis, Investigation, Data Curation **Drashtibahen Daraji:** Methodology, Validation, Formal analysis, Investigation **Charles Lail III:** Methodology, Validation, Formal analysis, Investigation **Bart L. Staker**: Resources, Methodology, Validation, Formal analysis, Investigation, Data Curation, Writing - Review & Editing **Elijah L. Woodward**: Methodology, Validation, Formal analysis, Investigation, Data Curation **Linjun Liu**: Methodology, Validation, Formal analysis, Investigation, Data Curation **Kevin P. Battaile**: Methodology, Validation, Formal analysis, Investigation, Data Curation **Scott Lovell**: Resources, Methodology, Validation, Formal analysis, Investigation, Data Curation, Writing - Original Draft, Writing - Review & Editing, Supervision **Timothy J. Hagen**: Conceptualization, Project administration, Writing - Review & Editing, Supervision **Damian J. Krysan**: Conceptualization, Project administration, Writing - Review & Editing, Resources, Supervision, Funding Acquisition